PERGAMON

International Journal of Solids and Structures 40 (2003) 1265–1280

INTERNATIONAL JOURNAL OF SOLIDS and STRUCTURES

www.elsevier.com/locate/ijsolstr

Wind–rain-induced vibration of cable: an analytical model (1)

Lingyun Wang *, Y.L. Xu

Department of Civil and Structural Engineering, Hong Kong Polytechnic University, Hung Hom, Kowloon, Hong Kong

Received 4 August 2001; accepted 3 September 2002

Abstract

There have been many reports recently on excessive and unanticipated vibration of cables in cable-stayed bridges under the simultaneous occurrence of wind and rain. Correspondingly, many efforts have been made to avoid such large amplitude cable vibrations that often cause fatigue damage and corrosion to strands in surprisingly short periods. However, the mechanism of wind–rain-induced cable vibration is still not clear and the analytical solution is being actively sought for the design of cables against such a vibration. This paper thus presents a preliminary theoretical study aiming to provide an analytical solution to the problem and to explain some phenomena observed from field measurements and wind–rain tunnel tests. The proposed analytical model takes into account the effect of mean wind speed on the position of upper rivulet and the influence of moving upper rivulet on cable vibration. The analytical model is then verified through the comparison with the simulated wind tunnel tests for cables with moving rivulet or fixed artificial rivulet. It turns out that the analytical model can capture main features of wind–rain-induced cable vibration. The comparative studies also shed light on the mechanism of wind–rain-induced cable vibration.
© 2002 Elsevier Science Ltd. All rights reserved.

Keywords: Stayed-cable; Cable vibration; Wind; Rain; Moving rivulet; Fixed rivulet; Analytical model; Comparison

1. Introduction

There have been many reports recently on excessive and unanticipated vibration of stay cables in cable-stayed bridges under the simultaneous occurrence of wind and rain. Such large amplitude cable vibrations due to wind and rain often cause fatigue damage and corrosion to strands in surprisingly short periods. The impact between two adjacent cables also arouses serious human anxiety. Many studies have been thus carried out to try to find out the reason behind this type of vibration and the measures for mitigating such a vibration.

Hikami and Shiraishi (1988) carried out field measurement of stayed cables in the Meikonishi Bridge subject to wind with and without rain. They found that the cables, which were of small amplitude vibration under wind without rain, became very unstable under wind but with rain. They then conducted a series of wind tunnel tests with rain condition simulated and reproduced wind–rain-induced cable vibration in their model tests. They concluded that the rivulet formed along the upper surface of a cable under the action of

* Corresponding author. Fax: +852-234-6389.
E-mail address: 98901561r@polyu.edu.hk (L. Wang).

0020-7683/02/$ - see front matter © 2002 Elsevier Science Ltd. All rights reserved.
PII: S0020-7683(02)00582-6

both wind and rain changed the original cable cross section and resulted in unstable cable vibration. Matsumoto et al. (1992) further conducted extensive wind–rain tunnel tests and pointed out that wind–rain-induced cable vibration was due to two major factors: one was the formation of upper rivulet and the other was the axial flow generated in the wake of the cable. Bosdogianni and Oliver (1996) compared wind tunnel results of cables with moving rivulet with those of the same cables but with fixed rivulet. They concluded that it was the presence of rivulet at a certain position and not the motion of rivulet that caused cable instability. However, Ruscheweyh (1999) did not agree with such a point of view. He stated that the rhythmic movement of rivulet was the "trigger" for wind–rain-induced cable vibration. He further stated that if the movement of rivulet could be stopped, rain–wind-induced cable vibration would stop.

Compared with the field measurements and wind–rain tunnel model tests of cables, theoretical studies towards the prediction of wind–rain-induced cable vibration are very limited. Yamaguchi (1990) presented a two-degree-of-freedom galloping model to describe wind–rain-induced cable vibration. In his model, the cable was regarded as a horizontal rigid cylinder without structural damping. The inertia moment due to the circumferential motion of the upper rivulet was considered in equilibrium with the aerodynamic moment on the cable. By using the quasi-steady assumption and the linearization technique, Yamaguchi (1990) derived the homogeneous second order linear differential equation of two degrees of freedom and carried out the complex eigenvalue analysis. He concluded that one-degree-of-freedom galloping theory might not be useful to explain the mechanism of wind–rain-induced cable vibration and the two-degree-of-freedom galloping theory should be applied. Geurts and van Staalduinen (1999), however, recently presented an engineering approach to the same problem but based on the one-degree-of-freedom galloping theory.

It is clear that wind–rain-induced cable vibration is a complicated solid–fluid-wind interaction problem. Its mechanism is not well understood yet. This paper thus presents a preliminary theoretical study aiming to explain and predict some phenomena of wind–rain-induced cable vibration observed from field measurements and wind–rain tunnel tests. The analytical model takes into account the interaction between wind, rivulet and cable. The circumferential oscillation of rivulet on the upper surface of the cable is quantified using the measured results reported in the literature. After the equation of motion for wind–rain excited cables is derived, the comparisons between theoretical and measured results are carried out for both cables with moving rivulet and cables with fixed artificial rivulet. The mechanisms of wind–rain-induced cable vibration are also explored in the comparative studies.

2. Analytical model

Let us use a rigid and uniform inclined cylinder to represent a stay cable segment (see Fig. 1a). The inclination of the cylinder is denoted by angle α, and the yaw angle of the incident wind is designated by angle β. The cylinder is supposed to be supported by springs at its ends in the plane 1-5-7. The consideration of such a cylinder rather than a real cable is because many researchers used it in their wind–rain simulation tests and some of the test results will be used in this paper for the verification of the analytical model. As a preliminary theoretical study, the upper rivulet is assumed to uniformly distribute along the longitudinal axis of the cylinder and circumferentially vibrate over the surface of the cylinder. Turbulent effect and axial flow effect are not considered. The static position of the upper rivulet due to the mean wind when the cylinder is stationary is defined by angle θ_0 and the dynamic angular displacement of the rivulet as the cylinder vibrates is designated by θ with reference to θ_0 (see Fig. 1b). Since the cylinder is not perpendicular to the direction of the mean wind speed U_0, one needs to find the component of mean wind speed perpendicular to the cylinder, U, using the following equation:

$$U = U_0\sqrt{\cos^2\beta + \sin^2\alpha\sin^2\beta} = U_0\sqrt{\sin^2\alpha + \cos^2\alpha\cos^2\beta} \tag{1}$$

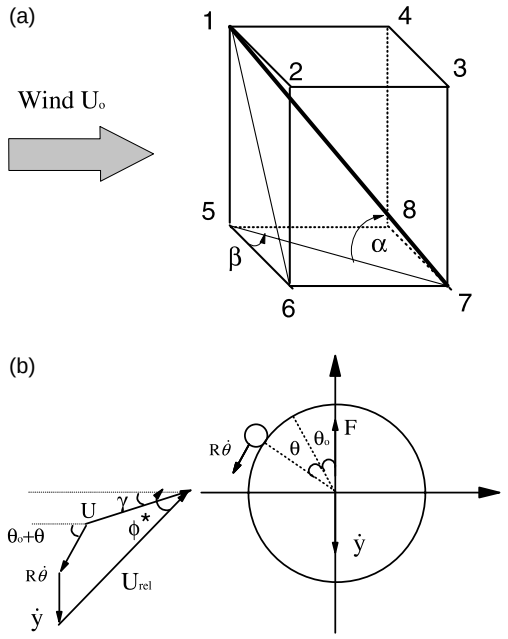

Fig. 1. Modeling of wind–rain-induced cable vibration: (a) orientation of inclined cylinder and (b) relative velocity of cable and moving rivulet.

The angle of attack of the mean wind speed component U is defined as γ (see Fig. 1b), which indicates the stagnation point of incident wind on the surface of cylinder. The position of stagnation point depends on many factors such as cross section of cylinder with rivulet, roughness of cylinder surface, wind turbulence, and cable motion. No experimental results are available to the writers at this stage with respect to the position of stagnation point on a stay cable with rivulet. Thus, the angle of attack in this study is selected as the ideal angle of attack multiplied by an influence factor ε.

$$\gamma = \varepsilon \sin^{-1}\left(\frac{\sin\alpha \sin\beta}{\sqrt{\cos^2\beta + \sin^2\alpha \sin^2\beta}}\right) \tag{2}$$

Clearly, when ε is set as 1, γ represents the ideal angle of attack for the cylinder without rivulet. When ε is selected as zero, it indicates that the position of stagnation point is the same as that on the ideal cylinder without rivulet and yaw angle. The effect of the position of stagnation point on wind–rain-induced cable vibration can be investigated in terms of the influence factor ε. The effects of the mean wind speed component along the cylinder axis and wind turbulence are not considered in this study.

In consideration of the transverse vibration of the cable of velocity $\dot{y}(t)$ and the angular vibration of the upper rivulet of velocity $\dot{\theta}(t)$, the relative velocity of mean wind to the cylinder with moving rivulet is therefore

$$U_{\mathrm{rel}} = \sqrt{(U\cos\gamma + R\dot{\theta}\cos(\theta+\theta_0))^2 + (U\sin\gamma + \dot{y} + R\dot{\theta}\sin(\theta+\theta_0))^2} \tag{3}$$

The angle between the relative velocity U_{rel} and the horizontal axis in Fig. 1b is defined as $\phi^*(t)$, which can be expressed as

$$\phi^* = \tan^{-1}\frac{U\sin\gamma + \dot{y} + R\dot{\theta}\sin(\theta+\theta_0)}{U\cos\gamma + R\dot{\theta}\cos(\theta+\theta_0)} \tag{4}$$

where R is the radius of the cylinder and the size of the rivulet is considered small compared with the diameter of the cylinder. The field and laboratory observations indicate that $R\dot{\theta}$ is very small compared with the concerned mean wind speed U. Thus, if the angles γ and $\phi^*(t)$ are limited a certain range, Eq. (4) can be reduced as

$$\phi^* \doteq \frac{U\sin\gamma + \dot{y} + R\dot{\theta}\sin(\theta+\theta_0)}{U\cos\gamma} \doteq \frac{U\sin\gamma + \dot{y} + R\dot{\theta}[(\theta+\theta_0) - \frac{1}{6}(\theta+\theta_0)^3]}{U\cos\gamma} \tag{5}$$

The net vertical force on the cylinder per unit length in the y-direction is then

$$F = \frac{\rho D U_{\text{rel}}^2}{2}[C_{\text{L}}(\phi)\cos\phi^* + C_{\text{d}}(\phi)\sin\phi^*] \tag{6}$$

where ρ is the density of the air; D is the diameter of the cross-section of the cylinder; C_{d} is the drag coefficient; and C_{L} is the lift coefficient. The drag and lift coefficients of the cylinder with rigid rivulet measured from the wind tunnel tests are often expressed as the function of the angle ϕ defined in Fig. 2 (e.g., Gu et al., 1999; Hikami and Shiraishi, 1988). The relationship between the angles ϕ^* and ϕ is given by

$$\phi = \phi^* - \theta - \theta_0 = \frac{U\sin\gamma + \dot{y} + R\dot{\theta}\left[(\theta+\theta_0) - \frac{1}{6}(\theta+\theta_0)^3\right]}{U\cos\gamma} - \theta - \theta_0 \tag{7}$$

In consideration that the cylinder structural damping is viscous and the cylinder mass is uniformly distributed, the equation of vertical motion of the cylinder can be written as

$$\ddot{y} + \omega^2 y + 2\xi_{\text{s}}\omega\dot{y} + \frac{F}{m} = 0 \tag{8}$$

In which ω is the circular natural frequency of the cylinder; ξ_{s} is the structural damping ratio of the cylinder; and m is the mass of the cylinder per unit length.

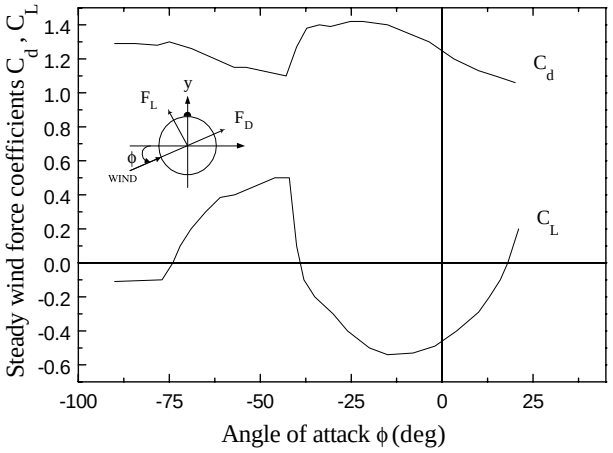

Fig. 2. Aerodynamic coefficients vs. wind angle of attack (Gu et al., 1999).

Now expand the drag coefficient and lift coefficient in Eq. (6) with respect to ϕ using the first three terms of the Taylor's series.

$$C_{\mathrm{L}}(\phi) = A_0 + A_1\phi + \frac{A_2}{2}\phi^2 + \frac{A_3}{6}\phi^3 \tag{9}$$

$$C_{\mathrm{d}}(\phi) = B_0 + B_1\phi + \frac{B_2}{2}\phi^2 + \frac{B_3}{6}\phi^3 \tag{10}$$

The substitution of Eqs. (9) and (10) into Eq. (6) and then the expansion of the sine and cosine functions in Eq. (6) with respect to ϕ^* using the first two terms of the power series yield the vertical force acting on the cylinder per unit length of the form.

$$F = \frac{\rho D U_{\mathrm{rel}}^2}{2}\left[\left(A_0 + A_1\phi + \frac{1}{2}A_2\phi^2 + \frac{1}{6}A_3\phi^3\right)\left(1 - \frac{\phi^{*2}}{2}\right) + \left(B_0 + B_1\phi + \frac{1}{2}B_2\phi^2 + \frac{1}{6}B_3\phi^3\right)\left(\phi^* - \frac{\phi^{*3}}{6}\right)\right] \tag{11}$$

The substitution of Eqs. (1), (3), (5) and (7) into Eq. (11) and then the reservation of the linear terms of $\dot{y}$, θ and $\dot{\theta}$ only lead to

$$F = \frac{\rho D}{2}(\Gamma_1 R U_0\dot{\theta} + \Gamma_2 U_0\dot{y} + \Gamma_3 U_0^2\theta) \tag{12}$$

where Γ_1, Γ_2, and Γ_3 can be found in Appendix. They are not only the function of the cable inclination, wind yaw angle, wind stagnation point, and the mean wind speed via the static position of rivulet but also the function of cable motion and rivulet motion which may change the values of drag coefficient and lift coefficient as indicated by Eqs. (7), (9) and (10). The combination of Eq. (8) with Eq. (12) results in

$$\ddot{y} + \omega^2 y + \left(2\xi_{\mathrm{s}}\omega + \frac{\rho D\Gamma_2 U_0}{2m}\right)\dot{y} = -\frac{\rho D}{2m}(\Gamma_1 R U_0\dot{\theta} + \Gamma_3 U_0^2\theta) \tag{13}$$

Based on the observations from either field measurements or simulated wind–rain tunnel tests, the motion of upper rivulet, θ, can be assumed to be harmonic (e.g., Hikami and Shiraishi, 1988), that is,

$$\theta = a\sin\widehat{\omega}t \tag{14}$$

The frequency of rivulet motion is almost the same as that of cable motion, as observed from wind–rain tunnel tests (Hikami and Shiraishi, 1988). The amplitude of rivulet motion, a, can be determined from wind–rain tunnel tests or by considering the circumferential motion of rivulet including factors, such as the size of rivulet and the roughness of cable surface. The first approach is adopted in this study for the time being while the second approach needs further investigation. Substituting Eq. (14) into Eq. (13) produces

$$\ddot{y} + \omega^2 y + 2\tilde{\xi}\omega\dot{y} = -\frac{\rho D a}{2m}(\Gamma_1 R U_0\widehat{\omega}\cos\widehat{\omega}t + \Gamma_3 U_0^2\sin\widehat{\omega}t) = \tilde{F}(t) \tag{15}$$

in which

$$\tilde{\xi} = \xi_{\mathrm{s}} + \frac{\rho D\Gamma_2 U_0}{4m\omega} = \xi_{\mathrm{s}} + \xi_{\mathrm{a}} \tag{16}$$

$\tilde{\xi}$ is the total damping ratio of the cylinder; ξ_{a} is the aerodynamic damping ratio; and $\tilde{F}(t)$ is the normalized force due to the motion of rivulet. Since Γ_2 changes with the mean wind speed U_0 through the static position of rivulet and depends on the motions of cable and rivulet, the aerodynamic damping ratio and the total damping ratio are the function of time. The conventional approach for predicting critical wind speed cannot be directly used in this study (Blevins, 1977).

3. Results and discussion

3.1. Horizontal cylinder with fixed rivulet

There are two approaches currently used by many researchers to simulate rivulet on cable section model in wind tunnel simulation tests: one is to spray water appropriately onto the surface of the cable model to form moving rivulet (e.g., Flamand, 1995), and the other is to stick artificial rivulet on the cable surface (e.g., Matsumoto et al., 1992; Gu et al., 1999). To start with the simplest case, this section investigates the dynamic behavior of horizontal cylinder with fixed rivulet using the derived formulation and then compares the results with the wind tunnel test results obtained by Gu et al. (1999).

When the rivulet is fixed, the dynamic motion $\theta(t)$ of the rivulet relative to the cylinder is equal to zero and the static position of the rivulet θ_0 is no longer the function of the mean wind speed. The equation of vertical motion of the horizontal cylinder becomes

$$\ddot{y} + \omega^2 y + 2\tilde{\xi}\omega\dot{y} = 0 \tag{17}$$

Γ_2 in Eq. (16) is also changed. For instance, Γ_2 can be expressed by the following equation for the horizontal cylinder with zero wind yaw angle β.

$$\Gamma_2 = B_0 - B_1\theta_0 + \frac{B_2}{2}\theta_0^2 - \frac{B_3}{6}\theta_0^3 + A_1 - A_2\theta_0 + \frac{A_3}{2}\theta_0^2 \tag{18}$$

For the cylinder with fixed rivulet, the coefficients A_i and B_i $(i = 1, 2, 3, 4)$ may change with the angle ϕ that in turn depends on the cylinder velocity $\dot{y}$ and the angle θ_0, as seen from Eqs. (7), (9) and (10). Therefore, Eq. (17) is a nonlinear differential equation. The Runge–Kutta method with the computer package MATLAB as a platform is employed to find the solution of the equation of motion of the cylinder with rivulet. The error coefficient in the computation is set as 10^{-7}.

Let us consider a horizontal cylinder of 120 mm diameter with a fixed upper rivulet, as investigated by Gu et al. (1999). The measured drag and lift coefficients are plotted in Fig. 2. It is seen that when ϕ is equal to $-43°$, the derivative of lift coefficient with angle of attack has a sudden change from a positive value to a negative value whereas the derivative of the drag coefficient changes from a negative value to a positive value. To have the best fit of the measured aerodynamic coefficients using the first three terms of the Taylor's series, the measured aerodynamic coefficients are divided into the two ranges distinguished by the critical angle ϕ of $-43°$. The coefficients A_i and B_i $(i = 1, 2, 3, 4)$ obtained from the best fit are listed in Table 1.

Fig. 3a shows the time history of displacement response of the horizontal cylinder with fixed rivulet, obtained by using Eqs. (7) and (16)–(18) with a small initial displacement. The cylinder has the following parameters: the mass per unit length of the cylinder m is 3.48 kg/m; the natural frequency f_n is 1.28 Hz; and the structural damping ratio ξ_s is 0.2%. The mean wind speed U_0 and yaw angle β are 10 m/s and zero, respectively. The air density is 1.225 kg/m^3 and the position of the fixed rivulet θ_0 is 32°. The computed result shows that after giving a small initial displacement, the vibration amplitude of the cylinder increases with time within the first 320 s. This is because the total damping ratio $\tilde{\xi}$ is negative and constant during this period (see Fig. 3d). After the amplitude of the cylinder is increased to a certain level, the angle ϕ reaches

Table 1
The coefficients in Taylor's series from the best fit of the measured results used for the case of fixed rivulet

Range	A_0	A_1	A_2	A_3	B_0	B_1	B_2	B_3
$\phi \geqslant -43°$	−0.48	0.84	4.69	0.86	1.25	−0.65	−0.08	6.81
$\phi < -43°$	2.19	5.89	14.06	17.53	−0.87	−5.97	−11.94	−12.18

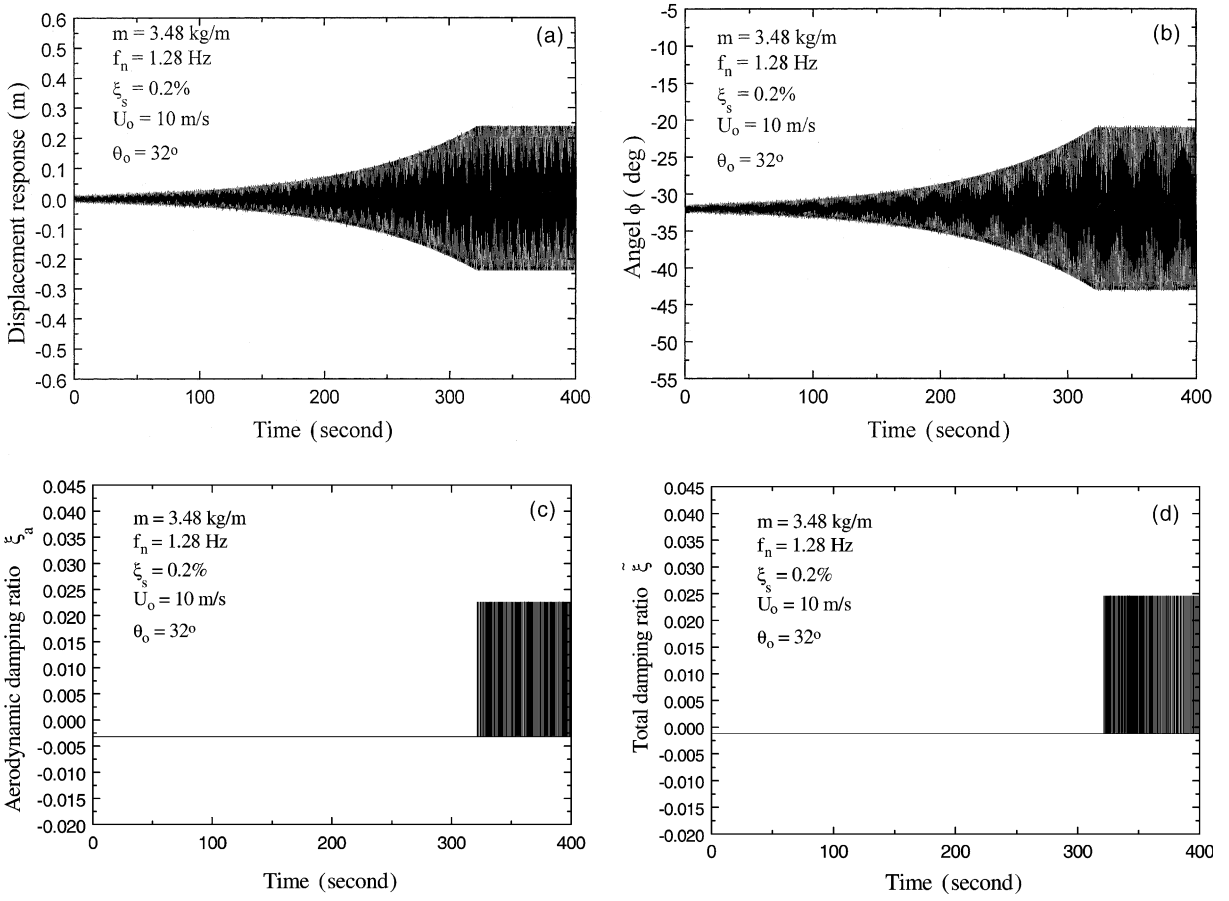

Fig. 3. Time histories of horizontal cylinder vibration with fixed rivulet: (a) displacement response, (b) angle ϕ, (c) aerodynamic damping ratio and (d) total damping ratio.

the value of −43° (see Fig. 3b). The aerodynamic damping ratio and the total damping ratio then change alternately between a negative value and a positive value rather than they remain constant (see Fig. 3c and d). As a result of the jump of aerodynamic damping, the motion of the cylinder becomes almost periodic with nearly constant peak-to-peak amplitude after 320 s. The maximum peak-to-peak amplitude of the cylinder in this case is more than three times of the diameter of the cylinder.

To know the effect of position of the fixed rivulet θ_0 on cylinder vibration and to compare the analytical results with the test results, the motion of the horizontal cylinder with and without wind yaw angle is computed against a series of angles θ_0. The computed results are plotted in Fig. 4a for the case of zero wind yaw angle and in Fig. 4b for the case of 30° wind yaw angle together with the test results (Gu et al., 1999). In both figures, $A_{\max}$ means the maximum peak-to-peak amplitude. A_{allow} means the allowable peak-to-peak amplitude that was set as 530 mm in the simulated wind tunnel tests. The mean wind speed U_0 is 18 m/s used in the computation. $A_{\max}/A_{\text{allow}}$ equal to one indicates that the vibration amplitude is larger than the allowable amplitude. It is seen that the computed and measured results both demonstrate that within a certain range of θ_0 the cylinder has large amplitude vibration, but out of this range the cylinder has very small vibration or the cylinder stops its vibration very fast after a small initial displacement or disturbance. The cylinder starts its large amplitude vibration at 30°, measured by the wind tunnel test and also predicted

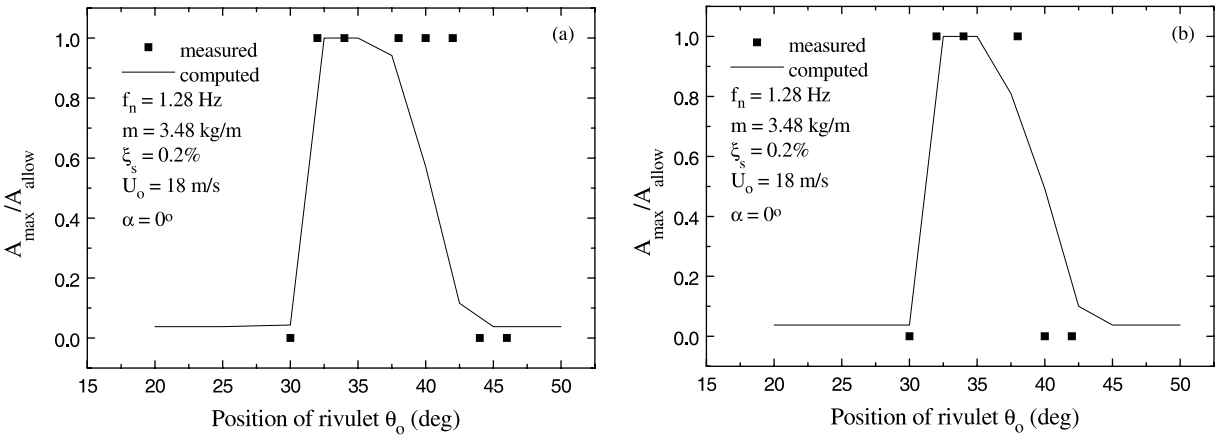

Fig. 4. Variation of cylinder vibration amplitude with position of upper rivulet: (a) zero wind yaw angle and (b) 30° wind yaw angle.

by the analytical model. There is some difference of the upper bound of the range between the computed and measured results but the difference is less than 5°.

Fig. 5a shows the variation of the normalized vibration amplitude of the cylinder with mean wind speed for the case of zero wind yaw angle and the rivulet position θ_0 of 32° whilst Fig. 5b shows the same quantities for the case of 30° wind yaw angle and θ_0 of 35°. Wind tunnel test results and analytical results are plotted together in these two figures. Again, the analytical results are in good agreement with the test results in both cases. In the case of the cylinder of zero wind yaw angle, it is seen that the large response amplitude of the cylinder occurs once if the mean wind speed reaches a certain level (onset wind speed). The large amplitude vibration remains with further increasing wind speed. This phenomenon somehow likes galloping vibration but in the analysis it is found that the response amplitude is actually limited though it is very large. In the case of the cylinder of 30° wind yaw angle, the wind tunnel test results and the computed results both show a kind of amplitude-restricted vibration. The reason why the vibration amplitude is limited is that when the vibration amplitude of the cylinder reaches a certain level, the aerodynamic damping ratio and the total damping ratio change periodically between a positive peak value and a negative

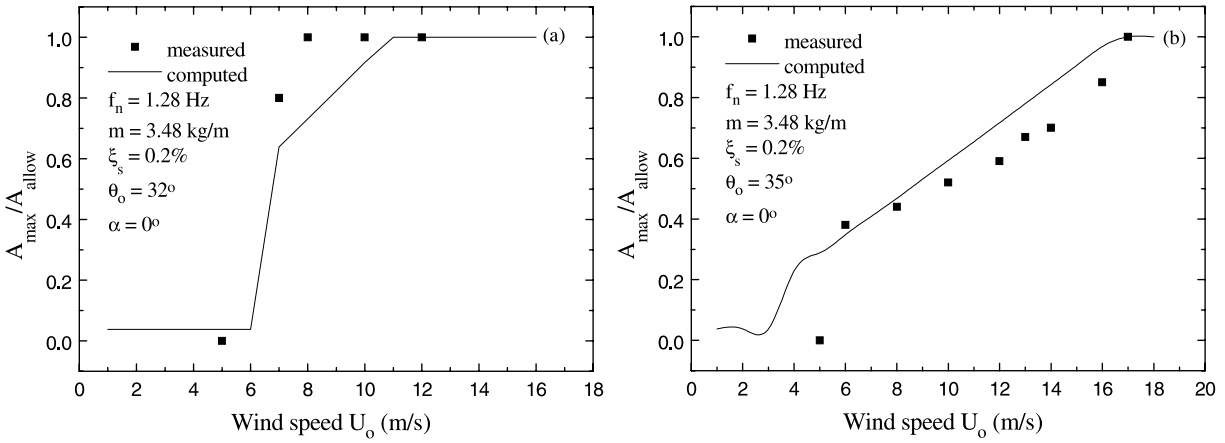

Fig. 5. Variation of cylinder vibration amplitude with mean wind speed: (a) zero wind yaw angle and (b) 30° wind yaw angle.

peak value. The onset wind speed predicted by the analytical model is slightly smaller than that measured from wind tunnel. As is reported by Matsumoto et al. (1992), the inclined cables with the fixed rivulet also show the velocity-restricted response at lower wind speed range that is due to certain vortex-shedding with much lower frequency than the Karmen vortex shedding.

3.2. Inclined cylinder with moving rivulet

To investigate the capability of the analytical model for predicting the motion of inclined cable with moving rivulet, the inclined cylinders tested in simulated wind–rain tunnels by Hikami and Shiraishi (1988) and by Ohshima and Nanjo (1987), respectively, are selected in this study. For the cylinder tested by Hikami and Shiraishi (1988), the drag and lift coefficient curves of the cylinder with upper rivulet ($d/D = 0.1$) were reported by Yamaguchi (1990) and reproduced in Fig. 6a. It is seen that there is a sudden change in the gradient of the curves at an angle of $-55°$. The curves are subsequently fitted to the Taylor's series of the first three terms distinguished by the critical angle of $-55°$. The resulting coefficients of the Taylor's series are listed in Table 2. For the moving rivulet, its static position θ_0 is the function of mean wind speed. The wind tunnel test results related to this position obtained by Hikami and Shiraishi (1988) are plotted in Fig. 6b and fitted by a quadratic function. The above drag and lift coefficients and the relationship between the static position of rivulet and wind speed are also applied to the inclined cylinder tested by Ohshima and Nanjo (1987), for these curves were not available from their paper.

The inclined cylinder tested by Ohshima and Nanjo (1987) has the following parameters (Case I): the diameter is 160 mm; the mass per unit length is 33.4 kg/m; both inclination and yaw angles are 45°; and the frequency is 1.62 Hz. Ohshima and Nanjo (1987) carried out 16 sets of tests with different rain conditions. Used in the comparison in this study is only the test under light rain condition (R-6). The test (R-6) was conducted using the structural damping factor δ of 0.002. The stagnation influence factor ε used in the computation is 0.7. The frequency of upper rivulet motion is assumed to be the same as the natural frequency of the cylinder, as observed by Hikami and Shiraishi from their tests (1988). The results obtained from the analytical model are showed in Fig. 7 together with the wind tunnel test results. In this figure, the x-coordinate is the mean wind speed U_0 and the y-coordinate is the maximum displacement response amplitude of the cylinder. Both analytical and measured results show that the wind–rain-induced cylinder vibration only occurs within a certain range of mean wind speed. The wind–rain-induced cylinder vibration

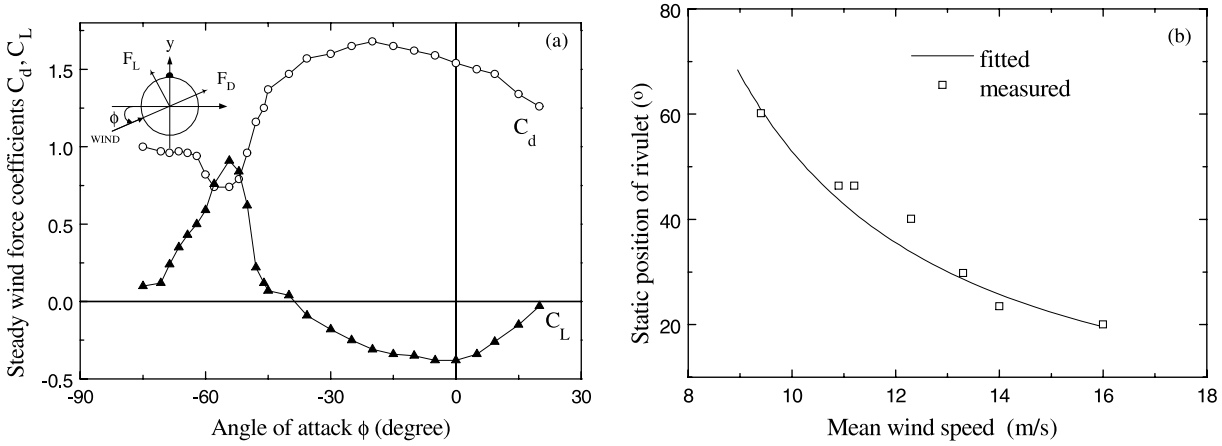

Fig. 6. Aerodynamic properties of wind–rain-induced cylinder vibration (Hikami and Shiraishi, 1988): (a) aerodynamic coefficients vs. wind angle of attack and (b) static position of upper rivulet vs. mean wind speed.

Table 2
The coefficients in Taylor's series from the best fit of the measured results used for the case of moving rivulet

Range	A_0	A_1	A_2	A_3	B_0	B_1	B_2	B_3
$\phi \geqslant -55°$	−0.42	0.64	3.46	−2.29	1.53	−0.72	−1.07	7.16
$\phi < -55°$	2.03	1.40	0	0	−5.08	−9.98	−8.12	0

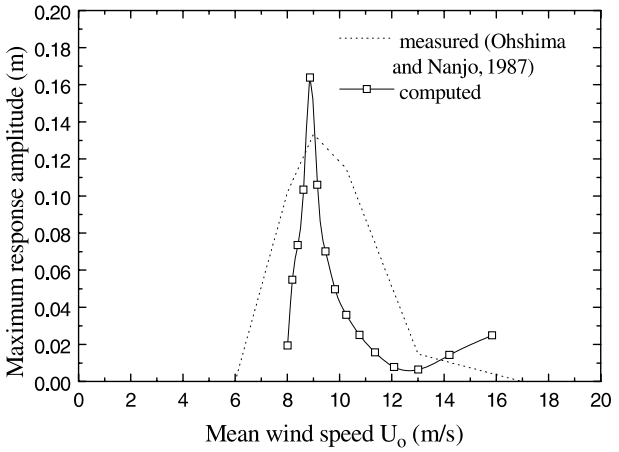

Fig. 7. Maximum cylinder vibration amplitude vs. mean wind speed (Case I).

is also a kind of vibration of restricted amplitude rather than galloping. The maximum vibration amplitude of the cylinder predicted by the analytical model is larger than that measured from the wind–rain tunnel tests. The on-set mean wind speed at which the cylinder vibration starts is lower in the wind tunnel tests than the computation. These differences may be due to many factors. For instance, the drag and lift coefficients and the relationship between the static position of rivulet and wind speed used in the computation were from the tests carried out by other researchers because Ohshima and Nanjo (1987) did not provide these data in their paper. The structural damping ratio of the cylinder used in the test is extremely small.

To explain why wind–rain-induced cylinder vibration is a kind of velocity and amplitude-restricted vibration, three particular mean wind speeds are selected to examine the inherent features of the corresponding cylinder vibration. These three mean wind speeds are 8.4 m/s corresponding to the vibration amplitude of medium level, 8.9 m/s related to the global maximum vibration amplitude, and 12 m/s at which the cylinder has very small vibration amplitude. For the mean wind speed of 8.4 m/s, the time histories of the computed angle $\phi(t)$, aerodynamic damping ratio $\xi_a(t)$, normalized force due to rivulet motion $\tilde{F}(t)$, and displacement response amplitude $y(t)$ are showed in Fig. 8a–d, respectively. It is seen from Fig. 8a that the angle $\phi(t)$ changes with time and the smallest amplitude is already less than −55°. This indicates that the rivulet is moving around the critical position where the gradients of the lift and drag coefficients of the cylinder change their signs. Correspondingly, the aerodynamic damping ratio ξ_a changes from the positive amplitude about 0.0014 to the negative amplitude about −0.0007 (Fig. 8b). After including the structural damping ratio, the amplitude of the total damping ratio $\tilde{\xi}(t)$ changes from the positive amplitude about +0.0017 to the negative amplitude about −0.0004. The normalized force $\tilde{F}(t)$ also changes with time because of the interaction between incident wind, moving rivulet and cylinder motion

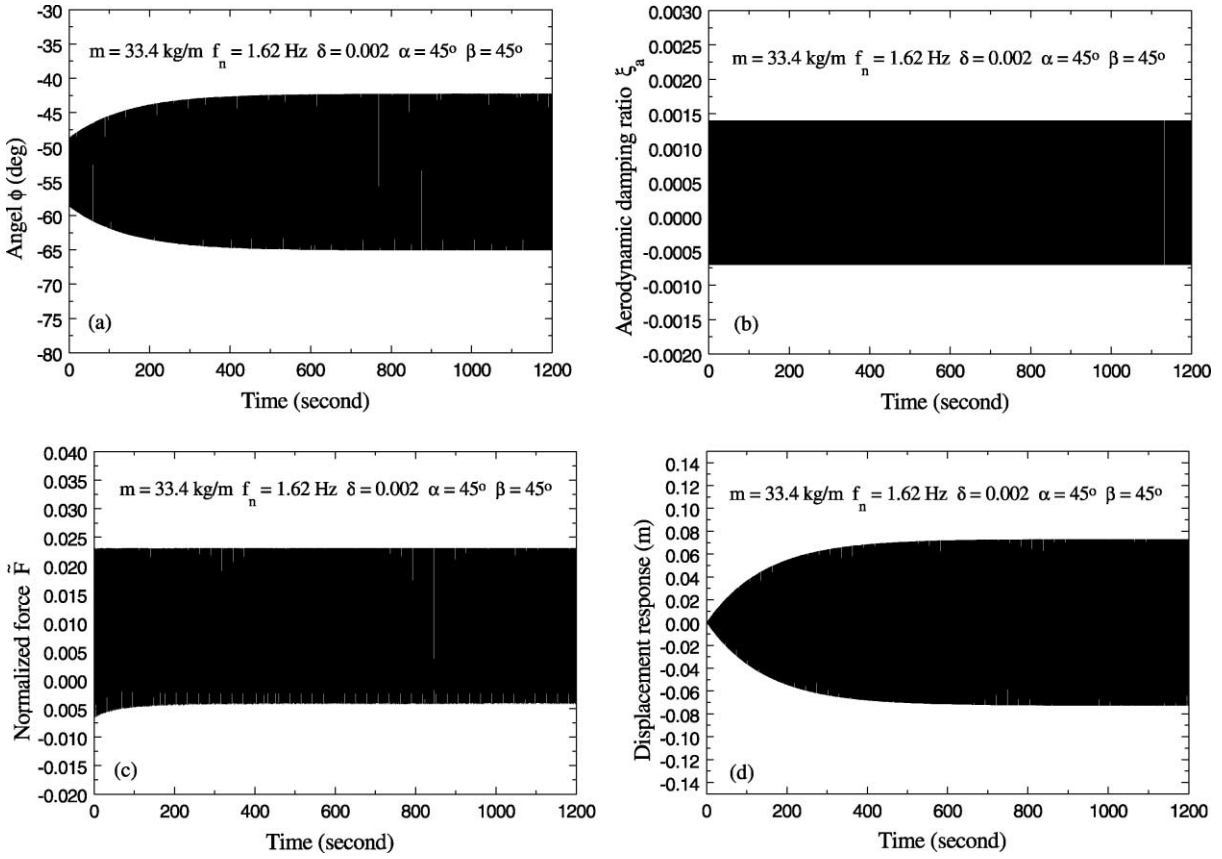

Fig. 8. Time histories of cylinder vibration (Case I, $U_0 = 8.4$ m/s): (a) angle ϕ, (b) aerodynamic damping ratio, (c) force due to rivulet motion and (d) displacement response.

(Fig. 8c). All these special features of wind–rain-induced cable vibration cause the cylinder to vibrate with almost constant restricted amplitude after a transient vibration period (Fig. 8d). The vibration amplitude is restricted and the maximum peak-to-peak amplitude is about 150 mm, about 94% of the cylinder diameter.

For the mean wind speed of 8.9 m/s, the time histories of the computed angle $\phi(t)$, aerodynamic damping ratio $\xi_a(t)$, normalized force due to rivulet motion $\tilde{F}(t)$, and displacement response amplitude $y(t)$ are showed in Fig. 9a–d, respectively. During the first 100 s, the cylinder vibration is in a transient vibration period. The smallest amplitude of the angle $\phi(t)$ is above $-55°$ (Fig. 9a). Therefore, the aerodynamic damping ratio and total damping ratio remain constant (Fig. 9b). The aerodynamic damping ratio and the total damping ratio are positive but very small during the first 100 s. The normalized force due to rivulet motion also changes with time but with the relatively large normalized peak-to-peak amplitude compared with the case of 8.4 m/s wind speed (Fig. 9c). Because of these factors, the cylinder vibration amplitude increases with time. When the vibration amplitude of cylinder increases to a certain level, the smallest amplitude of the angle $\phi(t)$ becomes less than $-55°$. The aerodynamic damping ratio and the total damping ratio no longer remain constant. Since the upper and lower bounds of the total damping ratio are quite small but the peak-to-peak amplitude of excitation force due to the motion of rivulet is relatively larger, the cylinder exhibits a large amplitude vibration of peak-to-peak amplitude about 0.34 m (Fig. 9d). Thus, one

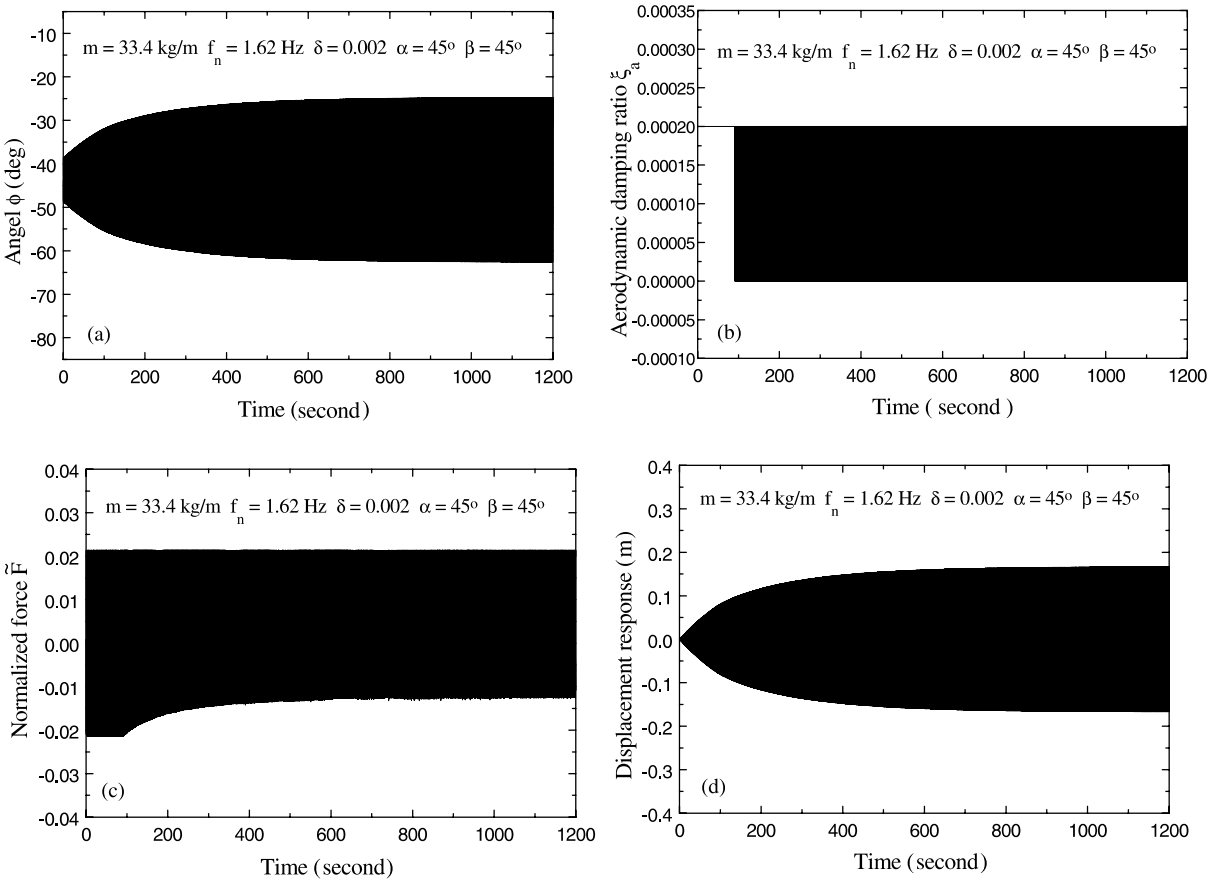

Fig. 9. Time histories of cylinder vibration (Case I, $U_0 = 8.9$ m/s): (a) angle ϕ, (b) aerodynamic damping ratio, (c) force due to rivulet motion and (d) displacement response.

may conclude that the restricted large amplitude vibration of the cylinder under 8.9 m/s wind speed is because of very small total damping ratio and relatively large amplitude force due to the motion of rivulet.

For the mean wind speed U_0 is 12 m/s, Fig. 10a–d display the time histories of the computed angle $\phi(t)$, aerodynamic damping ratio $\xi_a(t)$, normalized force due to rivulet motion $\tilde{F}(t)$, and displacement response amplitude $y(t)$, respectively. Since the angle $\phi(t)$ alters within the range much larger than $-55°$, both the aerodynamic damping ratio and the total damping ratio remain constant. The total damping ratio is 0.003, which is much larger than 0.0003 in the case of the cylinder under 8.9 m/s mean wind speed. On the other hand, the peak-to-peak amplitude of the normalized force due to rivulet motion is 0.011, which is much smaller than 0.034 in the case of the cylinder under 8.9 m/s mean wind speed. As a result, the vibration amplitude of the cylinder under 12 m/s mean wind speed is much smaller than that of the cylinder under 9.8 m/s mean wind speed.

The comparative study is also carried out using the inclined cylinder tested by Hikami and Shiraishi (1988) having the following parameters (Case II): the diameter is 140 mm; the mass per unit length is 10.2 kg/m; both inclination and yaw angles are 45°; and the natural frequency is 1 Hz. Unfortunately, the structural damping ratio was not explicitly given in the paper (Hikami and Shiraishi, 1988). It is thus assumed to be 0.7% together with the stagnation influence factor ε of 0.4. The frequency of upper rivulet

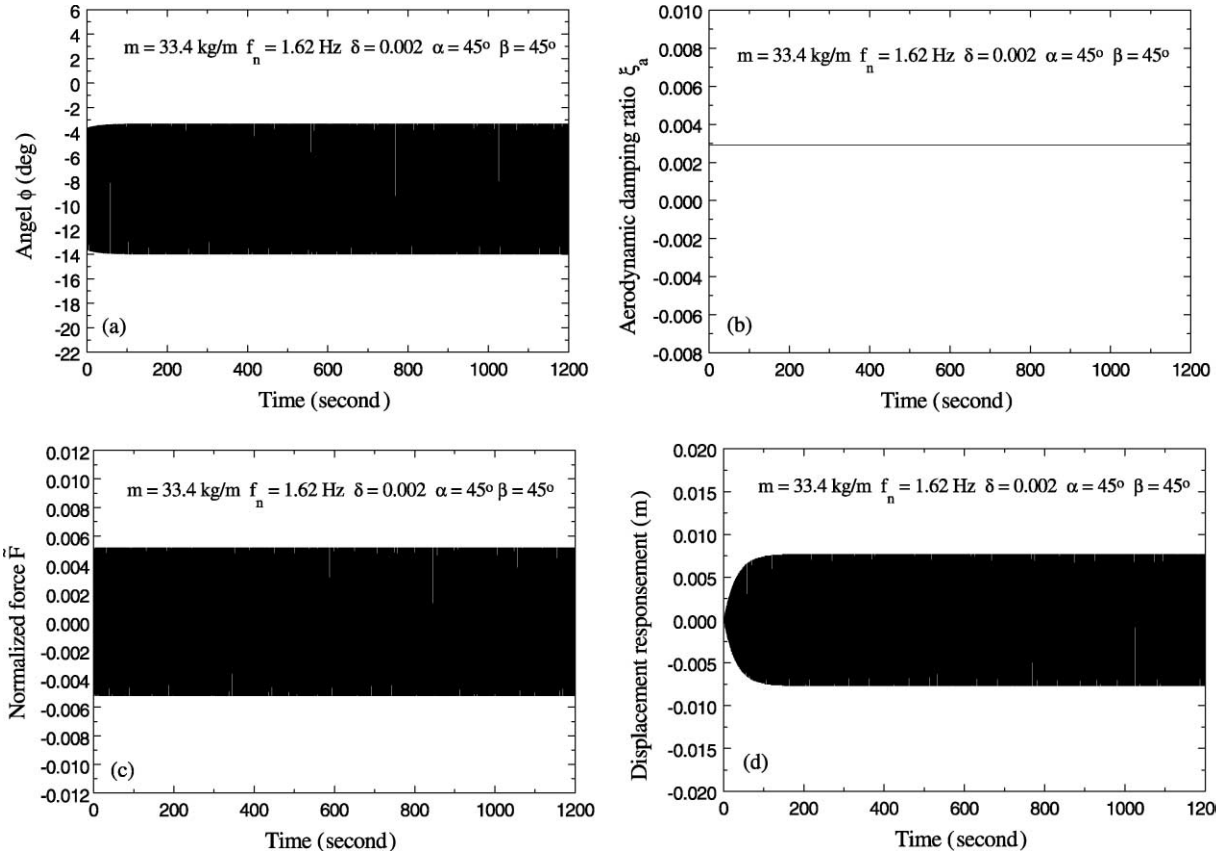

Fig. 10. Time histories of cylinder vibration (Case I, $U_0 = 12$ m/s): (a) angle ϕ, (b) aerodynamic damping ratio, (c) force due to rivulet motion and (d) displacement response.

motion is assumed to be the same as the natural frequency of the cylinder, as observed by Hikami and Shiraishi from their tests (1988). The results obtained from the analytical model are showed in Fig. 11 together with the wind tunnel test results. Again, both the computed results and test results exhibit the features of velocity and amplitude-restricted wind–rain-induced cable vibration. The predicted maximum vibration amplitude is, however, moderately larger than that from the wind tunnel tests. This may be due to uncertainties in the selection of stagnation influence factor and structural damping ratio. Two particular mean wind speeds, that is 9.8 and 12 m/s, are selected to examine cable vibration features. It is found that the basic features of wind–rain-induced vibration of the second cylinder are similar to those of the first cylinder as discussed before. At the mean wind speed of 9.8 m/s, the angle $\phi(t)$ changes with time and its negative amplitude is already less than $-55°$.

Thus, the aerodynamic damping ratio and the total damping ratio alternate with time. Because the structural damping ratio is relatively large in the second cylinder (Case II), the total damping ratio is kept within the positive value range although the low amplitude of the aerodynamic damping ratio is negative. The time-history of the displacement response of the cylinder is shown in Fig. 12a. When the mean wind speed is increased to 12 m/s, the low amplitude of angle $\phi(t)$ is always larger than $-55°$. Therefore, the aerodynamic damping ratio remains a constant negative value and the total damping ratio remains a constant small positive value. The cylinder vibration is periodic after the transient vibration period, as shown in Fig. 12b.

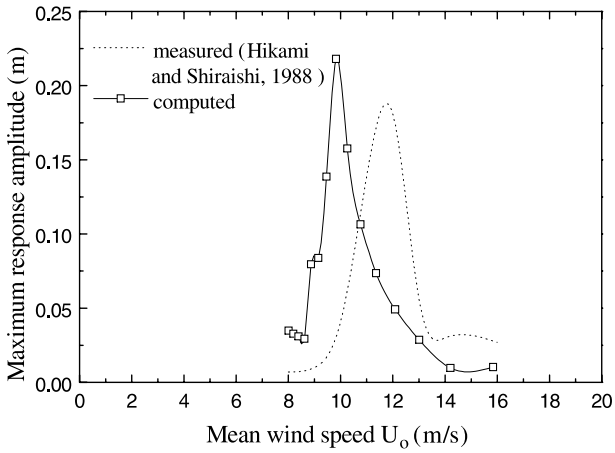

Fig. 11. Maximum cylinder vibration amplitude vs. mean wind speed (Case II).

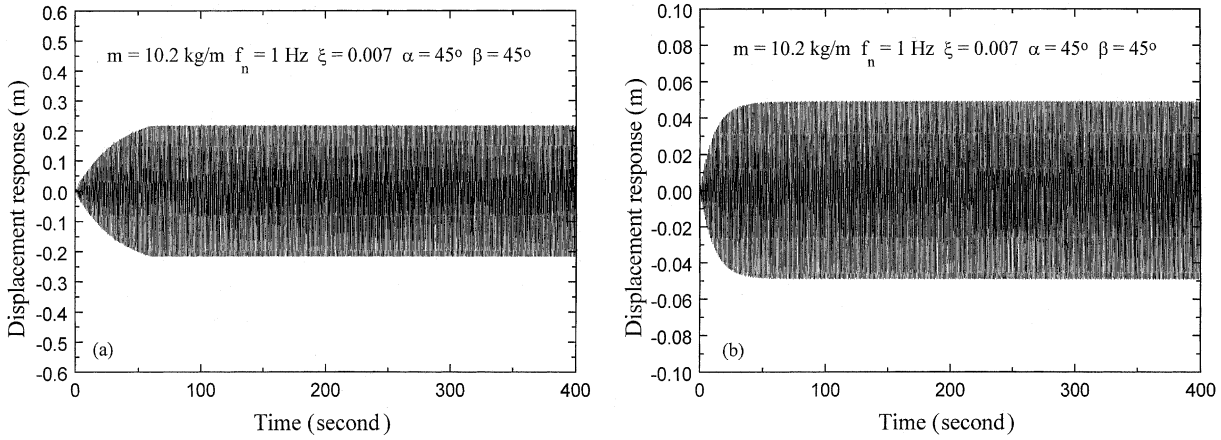

Fig. 12. Time histories of cylinder vibration (Case II): (a) mean wind speed U_0 of 9.8 m/s and (b) mean wind speed U_0 of 12 m/s.

The role of the rivulet movement for the velocity-restricted response of the cylinder is investigated to obtain the corresponding physical explanation. For the wind speed that is lower than the onset wind speed, the exciting force due to the rivulet motion is very small because of the small wind speed and the static position of rivulet under this wind speed. Then no wind–rain-induced vibration happens. If the wind speed increases, the negative aerodynamic damping occurs due to the wind speed and the corresponding static position of rivulet. The aerodynamic damping ratio then change alternately between a negative value and a positive value. As a result, the vibration of the system will be large but amplified-restricted. If the wind speed continues increasing, the exciting force due to the rivulet motion increases because of the increasing wind speed and the corresponding static position of the rivulet. Then the vibration mechanism here is some like the vortex shedding excited vibration. It suggests that the vortex shed from the system with the motion of the rivulet, which give the cylinder a periodic excitation. For the further increasing wind speed, the aerodynamic damping and total damping will be larger and larger due to the increasing wind speed. Then

the vibration amplitude of the system will reduce as the wind speed increases. Therefore, the wind–rain-induced vibration of the cylinder shows the velocity-restricted response.

4. Conclusions

An analytical model for describing wind–rain-induced cable vibration has been established in this paper. The effect of mean wind speed on the position of upper rivulet and the influence of moving upper rivulet on cable motion were taken into consideration in the model. The analytical model was then validated through the comparison with the wind tunnel simulation test results of cylinders with either moving rivulet or fixed artificial rivulet. It was found that the analytical model is able to capture main vibration features of inclined cylinders with moving rivulet, such as velocity-restricted vibration and amplitude-restricted vibration. The occurrence of velocity- and amplitude-restricted vibration is mainly because of alternating aerodynamic damping ratio and/or alternating excitation force due to the interaction between rivulet motion, cable motion and wind. The proposed analytical model can also predict the vibration of horizontal cylinder with fixed artificial rivulet. In this case, the vibration of large amplitude is due to negative aerodynamic damping ratio, but its vibration amplitude will be eventually restricted because the oscillation of cylinder leads aerodynamic damping ratio change within the range bounded by a negative value and a positive value.

It should be noted that the proposed analytical model is still a preliminary model. The axial flow and turbulence effects are neglected in this study. Some assumptions used in the model may be released in the further study. The systematic wind–rain tunnel simulation tests or field measurements guided by the proposed analytical model are needed.

Acknowledgement

The writers are grateful for the financial support from the Research Grants Council of Hong Kong through a RGC research grant (CERG 5066/97E).

Appendix A. Aerodynamic parameters $\Gamma_1 - \Gamma_3$

$$c_0 = \cos^2\beta + \sin^2\alpha\sin^2\beta \tag{A.1}$$

$$c_1 = [2 - (\gamma - \theta_0)^2]\sqrt{c_0} \tag{A.2}$$

$$c_2 = 2\sin\gamma\sqrt{c_0} \tag{A.3}$$

$$c_3 = \frac{1}{\sqrt{c_0}\cos\gamma} \tag{A.4}$$

$$c_4 = \frac{\theta_0 - \frac{\theta_0^3}{6}}{\sqrt{c_0}\cos\gamma} \tag{A.5}$$

$$c_5 = \tan\gamma \tag{A.6}$$

$$c_6 = c_5 - \theta_0 \tag{A.7}$$

$$\Gamma_1 = \left[c_0c_4\left(1-\frac{c_5^2}{2}\right)+c_1c_5\left(1-\frac{c_5^2}{6}\right)\right]B_0+\left[c_0c_4c_5\left(1-\frac{c_5^2}{6}\right)+c_0c_4c_6\left(1-\frac{c_5^2}{2}\right)+c_1c_5c_6\left(1-\frac{c_5^2}{6}\right)\right]B_1$$
$$+\left[c_0c_4c_5c_6\left(1-\frac{c_5^2}{6}\right)+\frac{c_0c_4c_6^2}{2}\left(1-\frac{c_5^2}{2}\right)+\frac{c_1c_5c_6^2}{2}\left(1-\frac{c_5^2}{6}\right)\right]B_2+\left[\frac{c_0c_4c_5c_6^2}{2}\left(1-\frac{c_5^2}{6}\right)\right.$$
$$\left.+\frac{c_0c_4c_6^3}{6}\left(1-\frac{c_5^2}{2}\right)+\frac{c_1c_5c_6^3}{6}\left(1-\frac{c_5^2}{6}\right)\right]B_3+\left[c_1\left(1-\frac{c_5^2}{2}\right)-c_0c_4c_5\right]A_0+\left[c_0c_4\left(1-\frac{c_5^2}{2}\right)\right.$$
$$\left.+c_1c_6\left(1-\frac{c_5^2}{2}\right)-c_0c_4c_5c_6\right]A_1+\left[c_0c_4c_6\left(1-\frac{c_5^2}{2}\right)-\frac{c_0c_4c_5c_6^2}{2}+\frac{c_1c_6^2}{2}\left(1-\frac{c_5^2}{2}\right)\right]A_2$$
$$+\left[\frac{c_0c_4c_6^2}{2}\left(1-\frac{c_5^2}{2}\right)-\frac{c_0c_4c_5c_6^3}{6}+\frac{c_1c_6^3}{6}\left(1-\frac{c_5^2}{2}\right)\right]A_3 \tag{A.8}$$

$$\Gamma_2 = \left[c_0c_3\left(1-\frac{c_5^2}{2}\right)+c_2c_5\left(1-\frac{c_5^2}{6}\right)\right]B_0+\left[c_0c_3c_5\left(1-\frac{c_5^2}{6}\right)+c_0c_3c_6\left(1-\frac{c_5^2}{2}\right)+c_2c_5c_6\left(1-\frac{c_5^2}{6}\right)\right]B_1$$
$$+\left[c_0c_3c_5c_6\left(1-\frac{c_5^2}{6}\right)+\frac{c_0c_3c_6^2}{2}\left(1-\frac{c_5^2}{2}\right)+\frac{c_2c_5c_6^2}{2}\left(1-\frac{c_5^2}{6}\right)\right]B_2+\left[\frac{c_0c_3c_5c_6^2}{2}\left(1-\frac{c_5^2}{6}\right)\right.$$
$$\left.+\frac{c_0c_3c_6^3}{6}\left(1-\frac{c_5^2}{2}\right)+\frac{c_2c_5c_6^3}{6}\left(1-\frac{c_5^2}{6}\right)\right]B_3+\left[c_2\left(1-\frac{c_5^2}{2}\right)-c_0c_3c_5\right]A_0+\left[c_0c_3\left(1-\frac{c_5^2}{2}\right)\right.$$
$$\left.+c_2c_6\left(1-\frac{c_5^2}{2}\right)-c_0c_3c_5c_6\right]A_1+\left[c_0c_3c_6\left(1-\frac{c_5^2}{2}\right)-\frac{c_0c_3c_5c_6^2}{2}+\frac{c_2c_6^2}{2}\left(1-\frac{c_5^2}{2}\right)\right]A_2$$
$$+\left[\frac{c_0c_3c_6^2}{2}\left(1-\frac{c_5^2}{2}\right)-\frac{c_0c_3c_5c_6^3}{6}+\frac{c_2c_6^3}{6}\left(1-\frac{c_5^2}{2}\right)\right]A_3 \tag{A.9}$$

$$\Gamma_3 = -c_0c_5\left(1-\frac{c_5^2}{6}\right)\left(B_1+B_2c_6+\frac{1}{2}B_3c_6^2\right)-c_0\left(1-\frac{c_5^2}{2}\right)\left(A_1+A_2c_6+\frac{1}{2}A_3c_6^2\right) \tag{A.10}$$

References

Blevins, R.D., 1977. Flow-Induced Vibration. Van Nostrand Reinhold, New York.

Bosdogianni, A., Oliver, D., 1996. Wind and rain induced oscillations of cables of stayed bridges. J. Wind Eng. Ind. Aerodyn. 64, 171–185.

Flamand, O., 1995. Rain-wind induced vibration of cables. J. Wind Eng. Ind. Aerodyn. 57, 353–362.

Geurts, C.P.W., van Staalduinen, P.C., 1999. Estimation of the effects of rain-wind-induced vibration in the design stage of inclined stay cables, In: Proc. 10th Int. Conf. Wind Eng., vol. 2, Denmark, Balkema, Rotterdom, pp. 885–892.

Gu, M., Xu, Y.L., Liu, C.J., Xiang, H.F. Response characteristics of wind excited cables with artificial rivulet. Submitted to J. Wind Eng. Ind. Aerodyn.

Hikami, Y., Shiraishi, N., 1988. Rain-wind induced vibrations of cables in cable stayed bridges. J. Wind Eng. Ind. Aerodyn. 29, 409–418.

Matsumoto, M., Shirashi, N., Shirato, H., 1992. Rain-wind induced vibration of cables of cable-stayed bridges. J. Wind Eng. Ind. Aerodyn. 41–44, 2011–2022.

Ohshima, K., Nanjo, M., 1987. Aerodynamic stability of the cables of a cable-stayed bridge subjected to rain, In: Proc. US–Japan Joint Seminar on Natural Resources, Japan, 324–336.

Ruscheweyh, H.P., 1999. The mechanism of rain-wind induced vibration, In: Proc. 10th Int. Conf. Wind Eng., vol. 2, Denmark, Balkema, Rotterdam, pp. 1041–1047.

Yamaguchi, H., 1990. Analytical study on growth mechanism of rain vibration of cables. J. Wind Eng. Ind. Aerodyn. 33, 73–80.